Chapter 1

Estimation of elastic constants in heterogeneous transversely isotropic media

Chapter 2 introduced the idea of fitting the traveltimes with elliptical velocity functions as a first step in the estimation of the elastic constants of a homogeneous TI medium. The techniques presented in chapters 3 and 4 (anisotropic ray tracing and anisotropic tomography) generalize to heterogeneous media the method of fitting the data with elliptical velocity functions. After fitting the traveltimes, the next step is the mapping from elliptical velocities to elastic constants. In this chapter, I show how all these techniques work together in the estimation of elastic constants in heterogeneous TI media.

1.1 Introduction

As chapter 2 shows, obtaining the elastic constants of a homogeneous TI medium from *P*-, *SV*- and, *SH*-wave traveltimes is a two-step procedure. The first step is to obtain direct and normal moveout (NMO) velocities by separately fitting traveltimes from each wave type with elliptical velocity functions. The second step is to map these elliptical velocities into elastic constants using equations (2.22) or (2.23). In this chapter I show that when the medium is heterogeneous, the elastic constants can be estimated by applying the procedure for homogeneous media many times to a heterogeneous model described as a superposition of homogeneous blocks. These blocks should incorporate our previous knowledge about the structure. The direct and NMO velocities needed at each block are estimated tomographically, as explained in chapter 4.

I start by explaining how the data aperture should be constrained to use the algorithm and how those constraints affect the estimation of both anisotropy and heterogeneity. Then I show the application of the technique using synthetic *P*- and

SV-wave traveltimes generated through a heterogeneous TI model. Finally, I present a field data example from a west Texas oil field. This example shows how the estimation of the elastic constants can add useful information when we study the properties of reservoir and nonreservoir rocks.

1.2 Aperture constraints: consequences

The procedure for estimating elastic constants from *P*-, *SV*- and *SH*-wave traveltimes can be summarized as tomographic estimation of elliptical velocities and transformation of the elliptical velocities into elastic constants. These two steps have opposite requirements in terms of data aperture. On the one hand, the mapping from elliptical velocities to elastic constants requires velocities estimated from rays that travel as closely as possible to one axis of symmetry, which is the assumption made in chapter 2 when deriving the equations that relate elliptical velocities and elastic constants. One the other hand, the tomographic estimation of elliptical velocities requires wide ray angles to improve the conditioning of the problem, the accuracy of the NMO velocities, and the spatial resolution of the result. Therefore, the aperture of the traveltimes used for the inversion should satisfy the following two conditions simultaneously: it shouldn't be too large because otherwise the elliptical approximation may not be adequate, and it shouldn't be too small because otherwise the tomographic estimation of elliptical velocities fails, even if the medium is actually isotropic.

Large ray angles are important for the estimation of moderate and large dips in the medium. Since the procedure doesn't allow the use of large ray angles in the inversion of *P*- and *SV*-wave traveltimes, I assume that the dips in the medium are small. If the dips are not small, they can be estimated first from *SH*-wave, wide-aperture traveltimes (that are truly elliptical), and the result can be used to constrain the boundaries in the inversion of *P*- and *SV*-wave data.

The axes of symmetry of the different homogeneous blocks that describe the model are assumed to be vertical or near vertical.[1] Therefore, when starting the iterations in the anisotropic traveltime tomography by assuming vertical axes of symmetry, the actual inclinations can be found while the estimation of the elliptical velocities remains accurate, regardless of the wave type. If the axes of symmetry are neither vertical nor close to vertical, we need to find their inclination first by fitting *SH*-wave traveltimes with heterogeneous elliptically anisotropic models, as explained in chapter 4. Once the inclination of the axes of symmetry of the different blocks is known, the elliptical group velocities of *P*- and *SV*-waves at each block are estimated using only rays that travel near the axes of symmetry. This process assumes that the axes of symmetry of the different blocks are in the same plane of the survey, as explained also in chapter 4.

In summary, in the absence of *SH*-wave traveltimes, the medium is assumed to

[1]They can also be horizontal or near horizontal. The algorithm works equally well in either case because the axes of symmetry of the ellipses are not constrained to be either the major or the minor axis, as explained in section 4.3.3, "Which is the axis of symmetry?."

be horizontally layered with vertical axes of symmetry. Small departures from this initial assumption can also be estimated. Larger variations from this initial guess require elliptical *SH*-wave traveltimes that allow the use of large data apertures.

When the inclination of the axes of symmetry varies across the medium, the estimated elastic constants are referred to different coordinate frames, one for each different axis of symmetry. For purposes of interpretation, having the elastic constants referred to different frames is not a problem as long as we also use the inclination of the axes of symmetry. However, for further computations (finite difference modeling, for example) it might be necessary to transform the elastic constants to a common frame. This transformation can be done by using Bond's matrices (Auld, 1990).

1.3 Synthetic example

P- and *SV*-wave synthetic traveltimes were generated using the anisotropic ray tracing algorithm described in chapter 3. Figure 1.1 shows the heterogeneous TI model where the rays were traced. This model shows the variation in depth of $V_{ij} = \sqrt{c_{ij}/\rho}$, the elastic constants transformed to velocity assuming unit density. The cross-well geometry used to compute the traveltimes consists of 92 sources and 92 receivers at each well. The distance between wells is 390 feet, and the separations between consecutive sources or receivers is 23 feet.

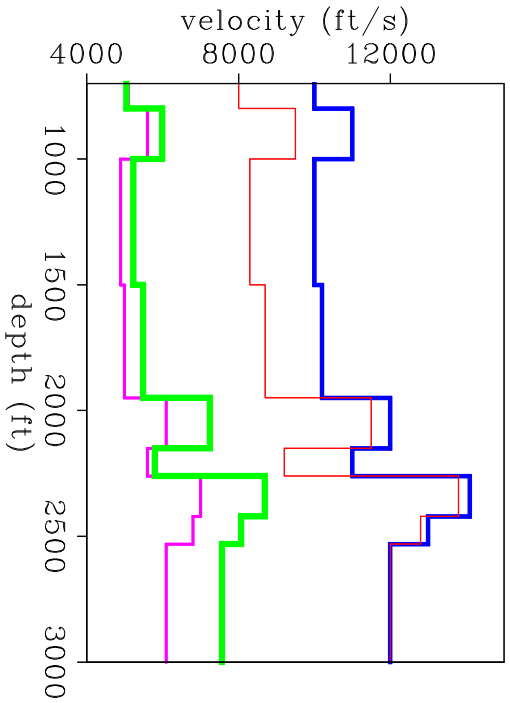

Figure 1.1: Layered TI synthetic model. From left to right the four curves represent the elastic constants in units of velocity V_{44}, V_{13}, V_{33}, and V_{11}, respectively. The density is assumed to be unity. elastic-exacto [NR]

Since the elastic constants of the medium are known, the corresponding elliptical velocities ($V_{P,x}$, $V_{P,z\text{NMO}}$, $V_{SV,x}$, and $V_{SV,z\text{NMO}}$) can be calculated easily by using the equations derived in chapter 2. Figure 1.2 shows the result. These velocities can be used to check how the algorithm performs in the first step toward the estimation of the elastic constants, that is, the tomographic estimation of the elliptical velocities.

As chapter 2 shows, the paraxial elliptical approximation around the horizontal axis (assuming vertical axis of symmetry) is accurate for angles of less than 30 degrees. For this reason, the inversion only uses rays whose angle measured from the horizontal satisfies this condition. However, no approximation is made in the computation of the synthetic traveltimes through the model of Figure 1.1. The paraxial approximation is made only during the inversion procedure in which the rays are traced in elliptically anisotropic instead of transversely isotropic models.

The fact that the straight line that connects a source-receiver pair forms a small angle with respect to the horizontal doesn't necessarily mean that the angle of the corresponding ray path is also small. The angle of the ray path increases in low-velocity layers and

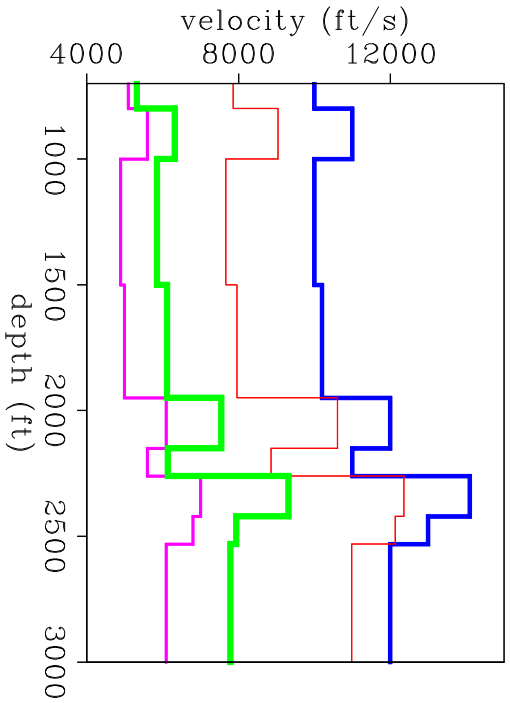

Figure 1.2: Theoretical elliptical velocities around the horizontal axis calculated from the elastic constants shown in Figure 5.1. From left to right the four curves represent $V_{SV,x}$, $V_{SV,z\mathrm{NMO}}$, $V_{P,z\mathrm{NMO}}$, and $V_{P,x}$, respectively. syn-ellip [NR]

decreases in high-velocity layers. However, if the velocity contrasts are not too strong, it should be enough to look at the straight line that connects source and receiver to select the rays that satisfy the proper constraints.

Figure 1.3 shows the result of inverting the P-wave traveltimes. This figure also shows the theoretical elliptical velocities calculated from the elastic constants. The estimation of the horizontal P-wave velocity is, as expected, almost perfect, whereas the vertical NMO velocity is slightly overestimated ($\approx 3\%$) in all layers. As Figure 1.4 shows, the estimation of the vertical NMO velocity is more accurate when inverting SV-wave traveltimes than when inverting P-wave traveltimes, which means that, for the range of ray angles used, the elliptical approximation works better for SV-waves than for P-waves. The error in $V_{SV,z\mathrm{NMO}}$ is less than one percent.

The errors in the NMO velocities $V_{P,z\mathrm{NMO}}$ and $V_{SV,z\mathrm{NMO}}$ come from using an elliptical approximation for ray angles that are not sufficiently small. When the model is truly elliptical, the estimation of the NMO velocities is accurate, as I show in chapter 4.

The variation with depth in the theoretical P- and SV-wave elliptical velocities has been estimated accurately. Therefore, by using these two models of elliptical velocities, we can also expect an accurate estimation of the elastic constants, as Figure 1.5 shows.

Since P- and SV-wave traveltimes are inverted separately and the interfaces are not constrained to move consistently with both data sets, the models obtained for P- and SV-wave elliptical velocities may not have all the interfaces at exactly the same depths. As a consequence, artificial thin layers (spikes) may appear when we

Figure 1.3: P-wave elliptical velocities. Dashed lines: result of the inversion of P-wave traveltimes with a ray angle of less than 30 degrees. Continuous lines: theoretical values. The curves with lower velocity correspond to $V_{P,z\mathrm{NMO}}$, and the ones with higher velocity correspond to $V_{P,x}$. syn-ellip-p [NR]

Figure 1.4: SV-wave elliptical velocities. Dashed lines: result of the inversion of SV-wave traveltimes with a ray angle of less than 30 degrees. Continuous lines: theoretical values. The curves with lower velocity correspond to $V_{SV,x}$, and the ones with higher velocity correspond to $V_{SV,z\mathrm{NMO}}$. syn-ellip-s [NR]

estimate the elastic constants because there may be slight relative mispositions of the same boundaries in the two models. In Figure 1.5 these spikes are removed by applying a median filter to the elastic constants after the mapping from elliptical velocities. Another way to solve this problem is by describing the interfaces with the same parameters for both P- and SV-wave velocity models and inverting the two sets of traveltimes simultaneously.

Depending on the radiation pattern of the source, traveltimes that correspond to nearly horizontal rays may not always be available for either P- or SV-waves. When this happens, it may be necessary to use ray angles that are far from the horizontal because nothing else is available. Figure 1.6 shows an example where SV-wave elliptical velocities have been estimated by using ray angles between 28 and 36 degrees. The estimated horizontal component of the velocity is as accurate as in Figure 1.4 even though this component is not well sampled by the ray paths used. The error in $V_{SV,z\text{NMO}}$ increases when using larger ray angles. However, as Figure 1.7 indicates, the error in the estimation of the elastic constants is still small because the P-wave elliptical velocities were estimated using small ray angles.

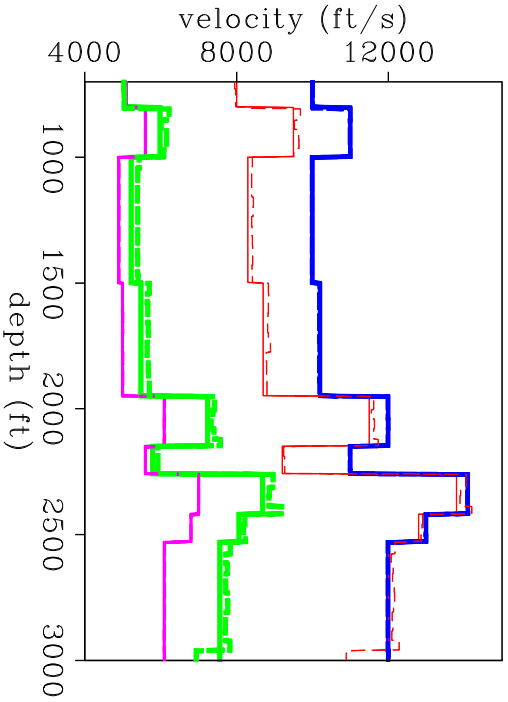

Figure 1.5: Elastic constants that control P- and SV-wave propagation. Dashed lines: estimated. Continuous lines: given. From left to right the four pairs of curves represent V_{44}, V_{13}, V_{33}, and V_{11}, respectively. exact-vs-approx-median [NR]

In the field data example that follows, SV-wave traveltimes are not available for small vertical offsets.

Figure 1.6: SV-wave elliptical velocities. Dashed lines: result of the inversion of SV-wave traveltimes with ray angles between 28 and 36 degrees. Continuous lines: theoretical SV-wave elliptical velocities. The curves with lower velocity correspond to $V_{SV,x}$ and the ones with higher velocity correspond to $V_{SV,z\text{NMO}}$. syn-ellip-s-28to36 [NR]

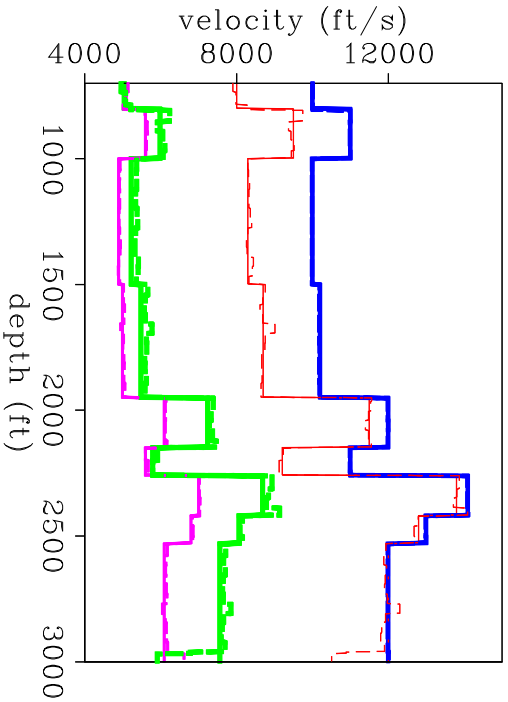

Figure 1.7: Elastic constants that control P- and SV-wave propagation. Dashed lines: elastic constants estimated when the ray angles used in the tomographic inversion of SV-wave traveltimes are between 28 and 36 degrees. The ray angles used to obtain the P-wave elliptical velocities are between 0 and 30 degrees, as in Figure 5.5. Continuous lines: original elastic constants. From left to right the four pairs of curves represent V_{44}, V_{13}, V_{33}, and V_{11}, respectively. exact-vs-approx-28to36 [NR]

1.4 Field data example

Cross-well data were recorded at the McElroy field, a carbonate reservoir of the Permian Basin in west Texas. This field has large oil reserves. It was discovered in 1926 and has been under continuous water-flooding since the early 1960s. McElroy field produces mainly from intertidal and shallow-shelf dolostones and siltstones of the Grayburg formation, which is a stratigraphic/structural trap. Hydraulic fracturing has stimulated reservoir performance. Porosity and permeability data from cores show that the Grayburg formation is very heterogeneous, with significant changes over short distances. The reason for the heterogeneity is that anhydrite and gypsum have plugged the pores (Avasthi et al., 1991). Structurally, the region is flat with mildly increasing dips at the bottom of the surveyed section (Lazaratos et al., 1992). The profile area is part of three 20-acre, five-spot patterns in a CO_2 pilot study.

A cylindrical piezoelectric bender was used as the source, a linear upsweep from 250 to 2000 Hz. Well spacing is 184 feet. The receiver well in the cross-well profiling was an observation well drilled for the CO_2 study, and the receiver system was a nine-level array of hydrophones. The plane of the survey is almost perpendicular to the direction of natural fractures measured in a nearby well (Avasthi et al., 1991). The target of the experiment was a reservoir between 1850 and 1960 feet. Sources and receivers were centered around the reservoir, from 1650 to 2150 feet.[2] The vertical spacing between sources and receivers was 2.5 feet. The survey consists of nearly 36 000 traces (201 sources $\times$ 178 receivers) sampled at 0.2 ms. More details about the data acquisition can be found in Harris et al. (1992).

Figure 1.8 shows a common receiver gather recorded at 1880 feet. Data editing and geometry definition was performed before picking the data. The total number of traveltimes picked from the field data was 33 519 and 20 887 for *P*-waves and *S*-waves, respectively. Van Schaack et al. (1992) show that the source can be modeled as a radial horizontal point source, which explains why no shear waves are clearly visible in the data for ray angles less than $\approx$ 28 degrees with respect to the horizontal, as Figure 1.8 shows.

P-wave energy is converted to shear energy at the source well. If the source well is perfectly cylindrical, and if the downhole source is positioned symmetrically within the source well, the polarization of the converted energy recorded at the receiver well is contained in the plane of the survey. Therefore, it is safe to assume that most of the recorded shear energy in this experiment corresponds to the *SV*-mode.

The *P*-wave traveltimes used for the inversion were from sources and receivers forming angles between 9 and 36 degrees with the horizontal. Even though the corresponding range of ray angles may be slightly different depending on how strong the velocity contrasts are, I still expect most ray angles at all layers to fall within the range of validity of the elliptical approximation. By applying this constraint on the data aperture, the number of *P*-wave traveltimes was reduced to 12 258 from the original 33 519. For similar reasons, the number of *S*-wave traveltimes was reduced

[2]Reservoir depths are changed for purposes of presentation in this chapter.

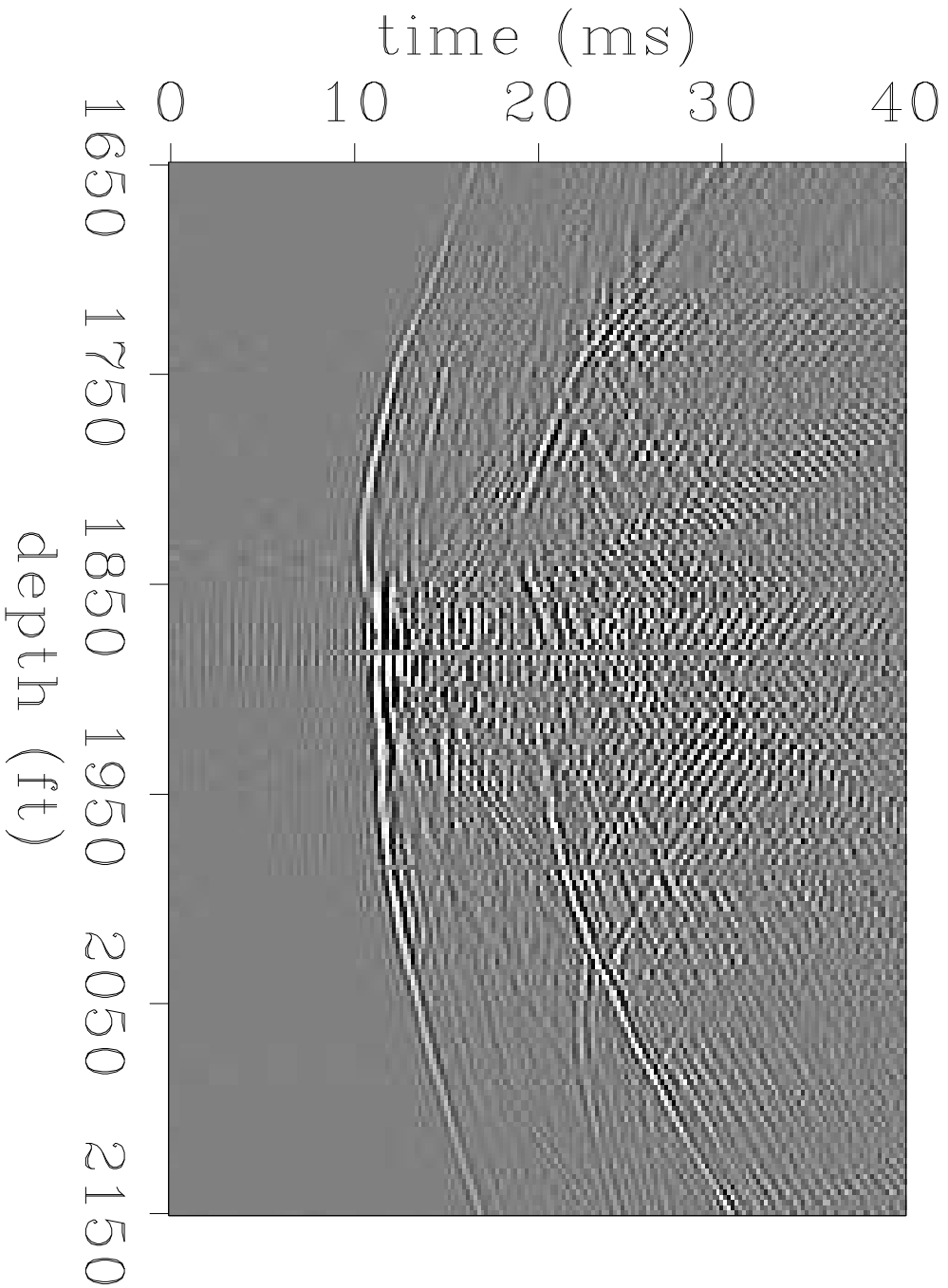

Figure 1.8: Common receiver gather recorded at 1880 feet. The source depth interval is 2.5 feet. The well-to-well separation is 184 feet. First arriving compressional and shear waves are clearly visible at most vertical offsets. Other wave modes are also visible. The target of the experiment was a reservoir between 1850 and 1960 feet. gather [NR]

to 2922, which corresponds to sources and receivers forming angles between 29 and 35 degrees.

The initial model for the tomographic inversion of P-wave traveltimes is homogeneous isotropic. The model is described by 200 horizontal layers of equal thickness (2.5 feet). Figure 1.9 shows the elliptical velocities that result after inverting the data. $V_{P,z\text{NMO}}$ is larger than $V_{P,x}$ in some strata, which indicates that the anisotropy is not caused by fine, horizontal layering, according to the results of section 2.7 "Constraints on elliptical velocities in layered media." The mean absolute value of the residuals [equation (??)] for this model is 0.086 ms.

Figure 1.9: P-wave elliptical velocities estimated from field data. Thick line: $V_{P,x}$. Thin line: $V_{P,z\text{NMO}}$. The model is described by 200 horizontal layers. mcroy-p [NR]

Figure 1.10 shows the elliptical velocities that result from the inversion of shear-wave traveltimes. The initial model in this case was also homogeneous isotropic and described by 200 layers of equal thickness. Seven layers were eliminated during the inversion procedure. $V_{SV,z\text{NMO}}$ is close to $V_{SV,x\text{NMO}}$, which means that, as discussed also in section 2.7, the P-wave anisotropy at this site is close to elliptical. As Figures 1.9 and 1.10 show, the shear-wave anisotropy at this site is smaller than the compressional wave anisotropy. The mean absolute value of the residuals computed for the model in Figure 1.10 is 0.240 ms, approximately equal to the sampling interval.

Finally, the elliptical velocities of Figures 1.9 and 1.10 are transformed into elastic constants by using equation (2.3) at each depth. Figure 1.11 shows the result of the transformation. V_{11} and V_{33} (horizontal and vertical P-wave velocities, respectively) vary more rapidly than V_{44} (SV-wave velocity). V_{33} is almost the same as $V_{P,z\text{NMO}}$ because the shear wave anisotropy is not significant, as Figure 1.10 shows. The

Figure 1.10: S-wave elliptical velocities estimated from field data. Thick line: $V_{SV,z\mathrm{NMO}}$. Thin line: $V_{SV,x}$. The model is described by 193 horizontal layers. mcroy-s [NR]

difference $V_{11} - V_{33}$ alternates between zero or negative in the interval between 1700 and 2100 feet. If we assume that the anisotropy is caused by fine layering, such changes in $V_{11} - V_{33}$ can be explained by a sequence of isotropic and anisotropic strata with horizontal axes of symmetry, probably vertically fractured. The reservoir between 1850 and 1960 feet corresponds to one stratum that is probably vertically fractured, which suggests that other intervals where $V_{11} < V_{33}$ may also correspond to vertically-fractured reservoir zones.

Figure 1.12 compares the horizontal and vertical velocities estimated from the cross-well measurements with the vertical shear and compressional velocities derived from the sonic log. Comparing shear-wave velocities yields the results expected for a TI medium: the vertical shear velocity from the sonic log is the same as the horizontal shear velocity derived from cross-well measurements. For the compressional velocities, however, the results are not as expected: the sonic log velocity is closer to the horizontal velocity than to the vertical velocity estimated from cross-well traveltimes.

The differences between vertical P-wave sonic velocity and vertical P-wave velocity estimated from cross-well traveltimes can be explained in several ways that are consistent with the idea of vertically fractured strata alternating with isotropic strata. One explanation is that fluids used when drilling can penetrate the reservoir zones causing a decrease in the compressional velocities of waves that travel close to the well without affecting either the velocities of waves that travel far from the well or the shear velocities. Another explanation assumes that the vertical fractures are

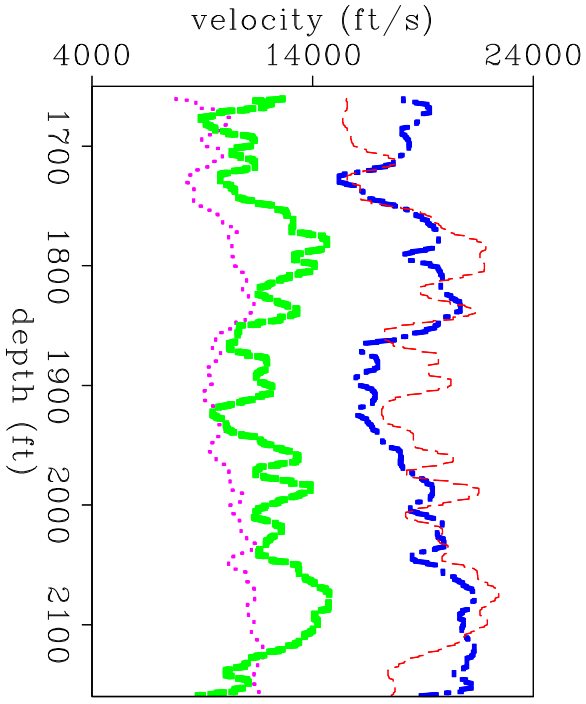

Figure 1.11: Elastic constants at the McElroy site (in units of velocity) estimated from the elliptical velocities of Figures 5.9 and 5.10, assuming a TI medium. Dotted line: V_{44}. Thick-dashed line: V_{13}. Dotted-dashed line: V_{11}. Thin-dashed line: V_{33}. mcroy-elastic [NR]

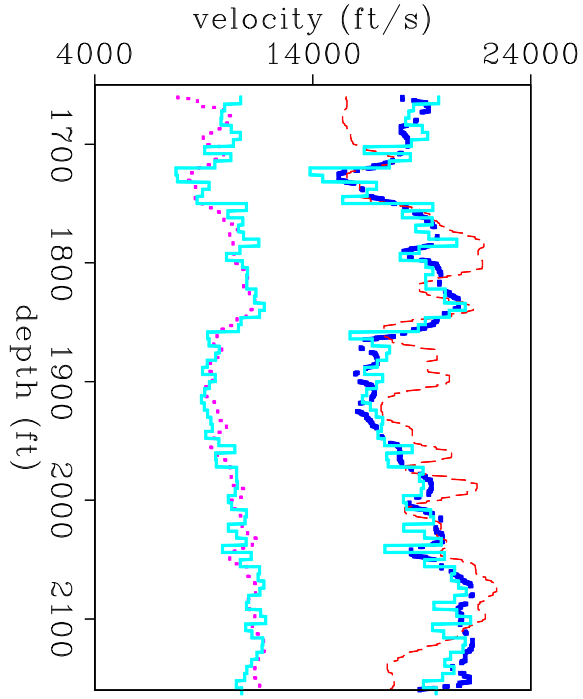

Figure 1.12: Elastic constants (in units of velocity) estimated from cross-well traveltimes compared with sonic logs blocked every six feet. Continuous line at the left: shear sonic velocity. Continuous line at the right: compressional sonic velocity. Dotted line: V_{44}. Dotted-dashed line: V_{11}. Thin-dashed line: V_{33}. mcroy-elastic-logs [NR]

embedded in a slow, fluid-filled matrix. The fractures are well-separated and filled with fast material (anhydrite), which can effectively increase the vertical velocity of waves that travel vertically in the interwell region without affecting either the velocity of waves that travel horizontally (because the fractures are thin) or the velocity of high-frequency waves that travel around the borehole in the low-velocity matrix. Strong, lateral heterogeneities in the vertical component of the velocity may cause the type of variation observed in the results, because the model doesn't account for them. This possibility, however, is less likely because reflection images of the site show fairly laterally homogeneous layers (Lazaratos et al, 1992).

Having out-of-plane shear arrivals would help to confirm the hypothesis of vertical fractures, by allowing us to look at the shear-wave splitting in the near horizontal direction.

1.5 Conclusions

The procedure used to estimate elastic constants in heterogeneous TI media is a generalization of the technique presented in chapter 2 for estimating elastic constants in homogeneous TI media. For homogeneous media, traveltimes from different wave types are fitted with elliptically anisotropic models. The elliptical velocities that result are then transformed into elastic constants. For heterogeneous media, the elliptical fit is performed by using anisotropic traveltime tomography, and the transformation to elastic constants is performed locally at each point in space.

The examples presented in this chapter show that the procedure is accurate as long as the maximum aperture satisfies the following constraints: it must be not too small because that would impede the estimation of the NMO velocities and not too large because the elliptical approximation might not be adequate.

In this chapter, I tested the algorithm with simple layered models. The estimation of elastic constants in media with more complex heterogeneities may require traveltimes from wider apertures, which could yield in less accurate results. This problem can solved by using traveltimes from all wave types from different recording geometries.